10-7-2021

Initial Acoustoelastic Measurements in Olivine: Investigating the Effect of Stress on P- and S-Wave Velocities

Taryn K. Traylor
University of Nevada, Las Vegas

Pamela C. Burnley
University of Nevada, Las Vegas, pamela.burnley@unlv.edu

M. L. Whitaker
Stony Brook University

Repository Citation

Traylor, T. K., Burnley, P. C., Whitaker, M. (2021). Initial Acoustoelastic Measurements in Olivine: Investigating the Effect of Stress on P- and S-Wave Velocities. *Journal of Geophysical Research: Solid Earth, 126*(11), 1-16.
http://dx.doi.org/10.1029/2021JB022494

JGR Solid Earth

RESEARCH ARTICLE
10.1029/2021JB022494

Key Points:

- We have experimentally measured the acoustoelastic effect in olivine at high pressure and temperature
- *P*-waves propagating along the axis of compression have a greater acoustoelastic sensitivity than *S*-waves
- Changes in the acoustoelastic constants as a function of pressure and temperature parallel those of the bulk and shear modulus

Supporting Information:

Supporting Information may be found in the online version of this article.

Correspondence to:

P. C. Burnley,
pamela.burnley@unlv.edu

Citation:

Traylor, T. K., Burnley, P. C., & Whitaker, M. L. (2021). Initial acoustoelastic measurements in olivine: Investigating the effect of stress on *P*- and *S*-wave velocities. *Journal of Geophysical Research: Solid Earth*, *126*, e2021JB022494. https://doi.org/10.1029/2021JB022494

Received 26 MAY 2021
Accepted 3 OCT 2021

Author Contributions:

Conceptualization: P. C. Burnley
Data curation: P. C. Burnley
Formal analysis: T. K. Traylor, P. C. Burnley, M. L. Whitaker
Funding acquisition: P. C. Burnley
Investigation: T. K. Traylor, P. C. Burnley
Methodology: T. K. Traylor, P. C. Burnley, M. L. Whitaker
Project Administration: P. C. Burnley
Resources: P. C. Burnley
Software: T. K. Traylor, M. L. Whitaker
Supervision: P. C. Burnley
Writing – original draft: T. K. Traylor
Writing – review & editing: P. C. Burnley, M. L. Whitaker

Initial Acoustoelastic Measurements in Olivine: Investigating the Effect of Stress on *P*- and *S*-Wave Velocities

T. K. Traylor[1], P. C. Burnley[1], and M. L. Whitaker[2]

[1]Department of Geoscience, University of Nevada, Las Vegas, Las Vegas, NV, USA, [2]Mineral Physics Institute, Stony Brook University, Stony Brook, NY, USA

Abstract It is well known that elasticity is a key physical property in the determination of the structure and composition of the Earth and provides critical information for the interpretation of seismic data. This study investigates the stress-induced variation in elastic wave velocities, known as the acoustoelastic effect, in San Carlos olivine. A recently developed experimental ultrasonic acoustic system, the Directly Integrated Acoustic System Combined with Pressure Experiments (DIASCoPE), was used with the D-DIA multi-anvil apparatus to transmit ultrasonic sound waves and collect the reflections. We use the DIASCoPE to obtain longitudinal (*P*) and shear (*S*) elastic wave velocities from San Carlos olivine at pressures ranging from 3.2–10.5 GPa and temperatures from 450–950°C which we compare to the stress state in the D-DIA derived from synchrotron X-ray diffraction. We use elastic-plastic self-consistent (EPSC) numerical modeling to forward model X-ray diffraction data collected in D-DIA experiments to obtain the macroscopic stress on our sample. We can observe the relationship between the relative elastic wave velocity change ($\Delta V/V$) and macroscopic stress to determine the acoustoelastic constants, and interpret our observations using the linearized first-order equation based on the model proposed by Hughes and Kelly (1953), https://doi.org/10.1103/physrev.92.1145. This work supports the presence of the acoustoelastic effect in San Carlos olivine, which can be measured as a function of pressure and temperature. This study will aid in our understanding of the acoustoelastic effect and provide a new experimental technique to measure the stress state in elastically deformed geologic materials at high pressure conditions.

Plain Language Summary Knowledge of the elastic properties of minerals is critical for understanding the structure and composition of Earth's interior and interpreting seismic data. This study investigates the effect of the stress state on *P*- and *S*-waves velocities; known as the acoustoelastic effect. To our knowledge, the acoustoelasticity of geologic materials at conditions relevant to Earth's interior has not been evaluated. This study focuses on olivine, a mineral that comprises a large portion of the lithospheric mantle. We use a D-DIA deformation apparatus to deform samples at high pressure and temperature while monitoring lattice parameters with synchrotron X-ray diffraction and the sample length with X-radiography. Simultaneously, we use ultrasonic interferometry to measure *P*- and *S*-wave travel times. We use these data to determine *P*- and *S*-wave velocities and the acoustoelastic effect as a function of pressure and temperature. We show that there is a measurable acoustoelastic effect in olivine that is nearly insensitive to changes in temperature and shows a minor pressure dependence. The effect is large enough that it may need to be considered in seismic data interpretation in regions where high stresses are present. Acoustoelastic properties may also be useful for directly measuring stress in lab-based experiments.

1. Introduction

The measurement of mineral elastic properties through experimental studies is crucial for seismic data interpretation and can aid in our understanding of the deformation processes that shape our Earth. Measurement of acoustic velocities, absolute pressure determination, and derivation of thermoelastic equations of state for various materials is traditionally done through experimental collection of ultrasonic interferometry measurements in conjunction with synchrotron X-radiation in a multi-anvil apparatus (Li et al., 2004). Lab-based elastic constants and velocity measurements are used by seismologists to interpret the Earth's interior, however, the constants describing the change in seismic velocity due to stress perturbation has yet to be measured at deep Earth conditions.

1.1. Stress-Induced Velocity Changes in Geologic Materials

The change in wave velocities that occurs when an elastic material is subjected to static stress, deemed "acoustoelasticity" in 1959 by Benson and Raelson, has been studied for over half a century. The idea of a stress-induced wave velocity change in a solid is derived from the photoelastic method of stress analysis in which a change in the index of refraction occurs when a polarized light beam propagates through a stressed optically transparent material (Benson & Raelson, 1959). As we will describe below, acoustoelasticity is the result of nonlinear elastic behavior. The nonlinear elastic behavior of rocks, as seen by departure from the generalized linear stress-strain relationship of Hooke's law, is well known (e.g., Birch, 1966; Johnson & Rasolofosaon, 1996; Winkler & Liu, 1996). The opening and closing of pre-existing cracks and damage at grain boundary contacts and crack tips are the typical causes of stress-induced velocity changes published in the literature for rocks. Previous geologic studies have derived the third-order elastic constants, using the theory of acoustoelasticity, for various sedimentary, igneous, and metamorphic rocks. The experiments in these studies are typically performed at ambient to low confining pressures (Liu et al., 2007; Lucet, 1989; Nur & Simmons, 1969; Winkler & Liu, 1996; Xie et al., 2018; Zamora, 1990).

Johnson and Rasolofosaon (1996) used the finite elastic deformation theory of Murnaghan (1951) to describe stress-induced velocity changes from published experimental data for sandstone and marble (Zamora, 1990), Barre granite (Nur & Simmons, 1969), and Bauvilliers limestone (Lucet, 1989). Johnson and Rasolofosaon (1996) observed that the third-order elastic constants are two to three orders of magnitude greater than the second-order elastic constants, which indicates a significant deviation from the linear stress-strain relationships at very small strain on the order of 10^{-3}.

Wang et al. (2015) developed a method, in the framework of the theory of acoustoelasticity, to determine the pressure in-situ during a high pressure-high temperature experiment using synchrotron X-radiation and ultrasonic interferometry. This method had success in determining the pressure, and identifying the presence of differential stress due to the apparatus configuration, in a Kawaii-type multi-anvil apparatus for a traditional ultrasonic experiment; these types of experiments collect ultrasonic measurements during the increase and decrease in confining pressure. However, Wang et al. did not quantify the acoustoelastic constants, nor did they perform experiments under uniaxial load.

1.2. Nonlinear Elastic Behavior of Solids

The classical linear theory of elasticity encompasses the generalized Hooke's law, where for infinitesimal deformation of an elastic material, the stress-strain relationship is expressed as a first-order approximation. This first-order theory is derived from expressing the strain-energy (W) function in terms of first- and second-degree strain (ε) products, with the corresponding first- and second-order elastic constants:

$$W = C_{ij}\varepsilon_{ij} + \frac{1}{2}C_{ijkl}\varepsilon_{ij}\varepsilon_{kl} \tag{1}$$

Differentiation of this expression with respect to strain, and the understanding that a material will not store energy if it is not deformed, results in an expression for stress in terms of strain and the second-order elastic constants:

$$\sigma_{ij} = C_{ijkl}\varepsilon_{kl} \tag{2}$$

Under this theory, P- and S-wave velocities remain constant when a stress is applied. However, it is known that a change in the state of stress does have an effect on wave velocities in solids, including rocks. Also, rocks may experience large deformations and behave plastically, resulting in violation of the assumptions of the linear elastic theory.

An extension of the linear elastic theory was proposed by Murnaghan (1951) to include finite deformation in elastically isotropic solids. This theory departs from the classical linear elasticity theory by first including higher-order terms in the strain energy function (to the third-order), and second, the resulting deformation is finite. For finite deformation, the initial and final coordinates of a point are now defined, and either set of coordinates may be used as the independent variables. Murnaghan's (1951) theory uses the Lagrangian system exclusively, in which the initial coordinates of a point are the independent variables. Murnaghan

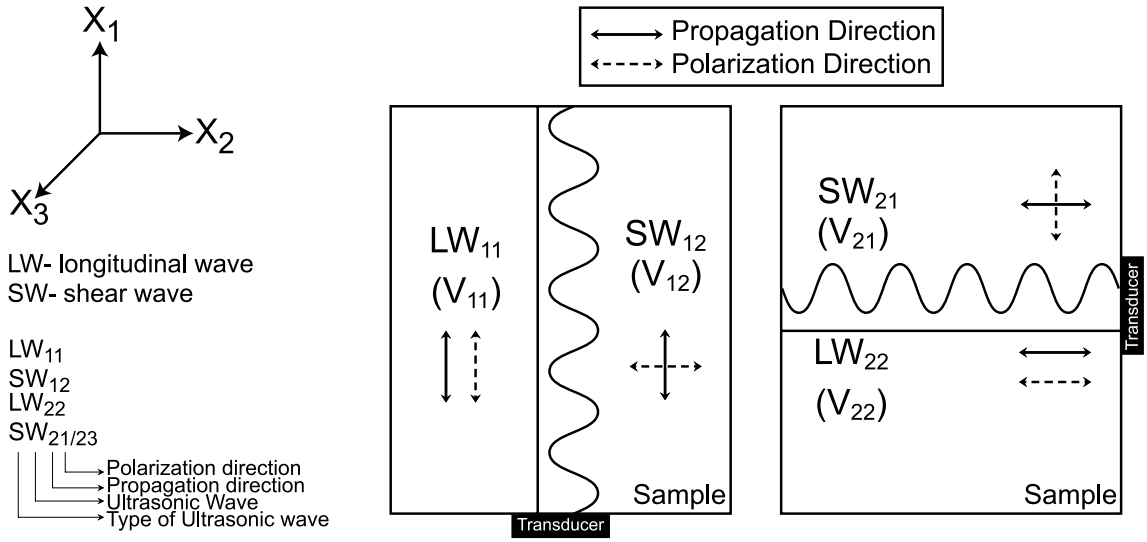

Figure 1. A schematic illustration of the various ultrasonic waves propagating from a single transducer placed along the X_1 axis of compression (left) and perpendicular to the X_1 axis of compression (right) (Modified from Bompan & Haach, 2018).

includes third-order elastic constants defined as *l*, *m*, and *n*, in addition to the Lamé second-order elastic constants, λ and μ. With terms in the strain energy function defined to the third-order, experimental determination of the third-order elastic constants has shown that we can use the acoustoelasticity theory to describe the dependence of ultrasonic wave velocities on the stress state as the waves propagate through a solid (Smith, 1963).

1.3. Acoustoelasticity

Previous studies have used acoustoelasticity to analyze the distribution of both residual and applied stress, in various materials such as metal, concrete, wood, and rocks, as well as to determine the third-order elastic constants. To study the acoustoelasticity of a material many theories of acoustoelasticity have been proposed, including Hughes and Kelly (1953), Toupin and Bernstein (1961), Thurston and Brugger (1964), Johnson (1981), Dey et al., (1984), and Man and Lu (1987). For this study, we use the Hughes and Kelly (1953) theory on the second-order elastic deformation of solids due to its applicability and ease of use, which we discuss below.

Hughes and Kelly (1953) formulated a series of empirical relationships (Equations 3a–3e) to calculate elastic *P*- and *S*-wave velocities in stressed solids using the nonlinear behavior laws derived by Murnaghan (1951). Hughes and Kelly evaluated *P*- and *S*-wave velocities as a function of stress for the case of hydrostatic pressure and uniaxial compression for polystyrene, Armco iron, and Pyrex glass. They used this data to determine the third-order elastic constants for each material. To determine Murnaghan's third-order elastic constants *l*, *m*, and *n* for an initially homogeneous isotropic material under uniaxial stress in principal direction one (Figure 1), the following equations are used:

$$\rho_0 V_{11}^2 = \lambda + 2\mu - \frac{\sigma_{11}}{3\left(\lambda + \frac{2}{3}\mu\right)}\left[2l + \lambda + \frac{\lambda + \mu}{\mu}\left(4m + 4\lambda + 10\mu\right)\right] \tag{3a}$$

$$\rho_0 V_{12}^2 = \mu - \frac{\sigma_{11}}{3\left(\lambda + \frac{2}{3}\mu\right)}\left[m + \frac{\lambda n}{4\mu} + 4\lambda + 4\mu\right] \tag{3b}$$

$$\rho_0 V_{22}^2 = \lambda + 2\mu - \frac{\sigma_{11}}{3\left(\lambda + \frac{2}{3}\mu\right)}\left[2l - \frac{2\lambda}{\mu}\left(m + \lambda + 2\mu\right)\right] \tag{3c}$$

$$\rho_0 V_{21}^2 = \mu - \frac{\sigma_{11}}{3\left(\lambda + \frac{2}{3}\mu\right)}\left[m + \frac{\lambda n}{4\mu} + \lambda + 2\mu\right] \tag{3d}$$

$$\rho_0 V_{23}^2 = \mu - \frac{\sigma_{11}}{3\left(\lambda + \frac{2}{3}\mu\right)}\left[m + \frac{\lambda + \mu}{2\mu}n - 2\lambda\right] \tag{3e}$$

where the elastic wave velocities (V_{ij}) contain subscripts 1, 2, and 3, with the first index denoting the direction of wave propagation and the second index denoting the direction of polarization, σ_{11} is the applied uniaxial compressive stress acting along the X_1 axis, λ and μ are the Lamé second-order elastic constants, and ρ_0 is the material density in the unstressed state. Equations 3c–3e are the only equations necessary to determine the third-order elastic constants, with Equations 3a and 3b providing a check on these values (Hughes & Kelly, 1953).

The acoustoelastic effect, the change in wave velocities due to the imposition of stress, is described by the acoustoelastic constants (A_{ij}) which can be derived by a linearization of the system of Equations 3a–3e above (Chaki & Bourse, 2009; Egle & Bray, 1976; Hughes & Kelly, 1953; Johnson et al., 1986; Lillamand et al., 2010). Thus:

$$A_{ij}\sigma_{11} = \frac{V_{ij}^{\sigma} - V_{ij}^{0}}{V_{ij}^{0}} \tag{4}$$

where σ_{11} is the applied uniaxial compressive stress acting along the X_1 axis, V_{ij}^{σ} is the wave velocity during deformation and V_{ij}^{0} is the wave velocity in the hydrostatic state before deformation, with i corresponding to the direction of propagation and j corresponding to the direction of polarization. Since V_{ij} is governed by the second-order and third-order elastic constants, the acoustoelastic constants are therefore, also a function of the second-order and third-order elastic constants. In this work, we will confine ourselves to the measurement of $A_{11,}$ which can be determined from measurements of the P-wave (LW_{11}) and $A_{12,}$ which can be determined from measurements of the S-wave (SW_{12}), as both waves propagate parallel to the applied stress.

1.4. Stress-Induced Velocity Changes in Metallic Materials

As previously mentioned, Hughes and Kelly (1953) experimentally confirmed their theory of acoustoelasticity through the determination of third-order elastic constants for various materials under uniaxial and hydrostatic compression. Researchers have since investigated a range of metallic materials (e.g., Bateman et al., 1961; Bergman & Shahbender, 1958; Crecraft, 1967; Egle & Bray, 1976; Nogueira, 2017; Rollins et al., 1963; Smith et al., 1966) using Hughes and Kelly's theory as well as alternative theories of acoustoelasticity mentioned above. Metallic material studies dominate a large portion of the acoustoelastic literature, primarily due to their importance in industrial uses. Many previous studies have used the theory by Hughes and Kelly (1953) to deduce the third-order elastic constants and have thus only used the equations involving the P- and S-wave velocities in the transverse direction to the applied stress (Equations 3c–3e). The following summarized studies have used an ultrasonic technique to evaluate the acoustoelasticity of a metallic material under the theory of Hughes and Kelly; in addition, a few of the studies have determined the acoustoelastic constants.

Crecraft (1967) showed that the acoustoelastic effect could be evaluated for various structural materials including nickel-steel, copper, and aluminum. In 1976, Egle and Bray experimentally derived the third-order elastic constants and the relationship between the relative wave velocity change and strain, rather than stress, which they termed "acoustoelastic constants" for samples of steel; this is in contrast to the above authors who have defined acoustoelastic constants as a function of stress. Egle and Bray measured all five possible wave velocities and calculated the "acoustoelastic constants" in two ways: (a) using equations 4a–4e stated in Egle and Bray (1976) which determined $\Delta V/V$ with axial strain using Poisson's ratio and the second- and third-order elastic constants, and (b) determining the slope of the relationship between $\Delta V/V$ and axial strain. The two calculations of the "acoustoelastic constants" agreed within the experimental error, showing that the first-order relationship between the measured $\Delta V/V$ and axial strain is adequate to

describe the stress dependence of wave velocity changes (see Figure S9 in the Supporting Information S1 for comparison of Egle and Bray (1976) measurements and olivine measurements of the current study in terms of the second method described above). In metallic materials, the third-order elastic constants are generally negative and approximately an order of magnitude greater than the second-order elastic constants. Using the second- and third-order elastic constants from the literature to calculate the acoustoelastic constants (see Table S5 in the Supporting Information S1), these calculated acoustoelastic constants for metals, in general, yield ~3% wave velocity change per GPa for *P*-waves and ~0.6% wave velocity change per GPa for *S*-waves, and are generally positive for both *P*-and *S*-waves propagating along the axis of compression.

1.5. General Objective

To our knowledge, the acoustoelasticity of geologic materials during a uniaxial deformation experiment at high pressure and high temperature conditions has not been evaluated. In addition, previous studies investigating the stress-induced wave velocity change in rocks, with the exception of Wang et al. (2015), have been conducted at low confining pressures where the primary mechanisms contributing to the relative wave velocity change are microcracking and porosity closure. The lack of high pressure acoustoelastic studies is attributed by Whitaker et al. (2017) to the inability of current ultrasonic interferometry technology to collect ultrasonic spectra fast enough to observe the time-dependent phenomena that occur during a high pressure-high temperature deformation experiment. In addition, the lack of integration of ultrasonic interferometry technology into a deformation experiment has delayed advancement in the study of the acoustoelastic effect. The current integration of the Directly Integrated Acoustic System Combined with Pressure Experiments (DIASCoPE) experimental acoustic system (Whitaker et al., 2017) into the D-DIA multi-anvil apparatus at the 6-BM-B synchrotron beamline at Argonne National Laboratory, Chicago, Illinois, allows us to investigate the acoustoelastic effect for two ultrasonic waves; a longitudinal (*P*) wave with propagation and polarization parallel to the applied compression direction (LW_{11}), and a shear (*S*) wave with propagation parallel to the applied stress and polarization normal to stress (SW_{12}). We present here an experimental study evaluating the acoustoelasticity of San Carlos olivine at lithospheric mantle pressure and temperature conditions. With pressure conditions ranging from 3.2–10.5 GPa, the results of this study, including the numerical value of the acoustoelastic constants for two samples of polycrystalline San Carlos olivine, to our knowledge, will be the first to directly quantify the acoustoelasticity of olivine at lithospheric mantle conditions.

2. Materials and Methods

The ultrasonics-modified deformation-DIA experiments were conducted using the D-DIA multi-anvil apparatus (Durham et al., 2002) and DIASCoPE acoustic system (Whitaker et al., 2017) located at the 6-BM-B beamline at the Advanced Photon Source at Argonne National Laboratory, Chicago, Illinois. The D-DIA multi-anvil apparatus combined with a synchrotron beamline provides the ability to measure sample stress and strain using in-situ X-ray techniques during the deformation experiment. The incorporation of the DIASCoPE acoustic system into a traditional D-DIA experiment allowed for simultaneous travel time measurements when deforming. Using the sample length measurements from synchrotron X-radiographic imaging and *P*- and *S*-wave travel times from the DIASCoPE, the elastic *P*- and *S*-wave velocities were determined. Powder diffraction data collected from the sample during deformation was then interpreted through elastic-plastic self-consistent (EPSC) modeling (Tomé & Oliver, 2002) following the strategies devised by Burnley (2015) and Burnley and Kaboli (2019) to determine the macroscopic stress on the sample. Correlating the elastic wave velocities with the macroscopic stress, the acoustoelastic constants (A_{ij}) were determined.

2.1. D-DIA Apparatus

The D-DIA multi-anvil apparatus is used to generate high pressure-high temperature conditions (Durham et al., 2002). Three tungsten carbide (WC) anvils and one sintered diamond anvil are horizontally distributed at 90°, and two WC anvils are vertically opposed (Figure S1 in the Supporting Information S1). To achieve high pressure conditions, the six anvils are simultaneously advanced by the main ram. The vertical anvils can then be independently displaced to uniaxially deform the sample, while the horizontal anvils retract to maintain a constant force and sample cell volume (Durham et al., 2002).

2.1.1. Sample Assembly Configuration

To integrate the DIASCoPE into a traditional D-DIA experiment, a hybrid sample assembly was developed that included aspects of an ultrasonics experiment and a deformation experiment (Figure S2 in the Supporting Information S1). The sample assembly used for each experiment is shown in the Supporting Information S1. A cubic pressure medium of mullite is used with an ~3 mm vertical hole drilled through the center. This hole accommodates a series of concentric sleeves consisting of a crushable alumina support sleeve, a thin walled graphite furnace and boron nitride (BN) confining media. In the center of the BN confining media, the sample, in series with a fully dense sintered alumina (Al_2O_3) upper piston, is enclosed within a 25 μm thick nickel sleeve. The sample consisted of pulverized San Carlos olivine that was isostatically hot-pressed at 1,150°C and 296.5 MPa for 8 h to produce an average grain size of ~8 μm (Figure S11 in the Supporting Information S1), cored to form a right cylinder, and then polished to ¼ μm to produce parallel ends. The nickel sleeve is used to help prevent the iron in the olivine from reducing. A cylinder of Coors AD-998 polycrystalline Al_2O_3 below the sample was used as a waveguide to couple the WC anvil to the sample and will be referred to as the buffer rod from now on. A crushable Al_2O_3 plug above the upper piston and BN sleeve was used to transmit the load from the top anvil. All surfaces intersecting the ultrasonic wave path were polished to 1 micron to ensure the interfaces were flat and parallel within 0.05°; the interfaces of the sample were polished to ¼ micron. 1 μm thick gold (Au) foils were placed at the sample interfaces, as well as the bottom anvil-buffer rod interface, to improve the coupling of these surfaces and minimize the loss of acoustic energy. In addition, the Au foils have a high X-ray absorption compared to the other cell materials, so the foils at the sample interfaces were used as strain markers in the X-radiographic images. A side-entry W 3%–W 25% Re thermocouple was inserted into the sample assembly to directly measure the sample temperature; the side entry placement was necessary to ensure that the thermocouple did not interfere with the ultrasonic wave travel path. However, the thermocouples are fragile and may break during the experiment. In experiment San_381, the thermocouple failed near the end of deformation sequence 2. Therefore, an extrapolation was made for the temperature for the remainder of the experiment by applying a polynomial fit to the thermocouple data prior to thermocouple failure (Figure S3 in the Supporting Information S1). As the thermocouple in San_416 did not work properly, we set the sample power level for each deformation sequence in San_416 to match the power level used in each San_381 deformation sequence, thus enabling comparison between the two experiments. For more information on the thermocouple set up and temperature uncertainty, please refer to the supplementary section.

2.2. Experimental Procedure

The San_381 experiment was compressed to ~7 GPa, at room temperature, as estimated by olivine diffraction. The sample was annealed at 1,000°C for ~1 h and 40 min to relax the stress in the grains developed during cold loading. During this annealing phase, grain growth started to occur, so the temperature was cooled to 850°C for the initial advance of the differential rams. Once the rams were in position to start the experiment, differential stress was observed again, so the temperature was raised to 980°C to relax the remaining differential stress. The total annealing process lasted 3 h and 26 min. The sample temperature was then lowered to the first experimental temperature of 450°C.

The San_416 experiment was compressed to ~10 GPa, at room temperature, as estimated by olivine diffraction. The temperature was then raised to 980°C and the sample was annealed for 43 min. Differential stress was still present, so the temperature was raised to 1,130°C for 37 min, and raised again to 1,240°C for 17 min. The total annealing process lasted ~1 h and 37 min. The sample temperature was then lowered to the first experimental temperature of 450°C.

The initial annealing phase allows the cell materials to extrude through the gaps between the anvils and relaxes the internal stresses within the cell assembly. This process results in a significant pressure loss. When the temperature is decreased to the experimental condition, the cell assembly pressure is further decreased due to thermal contraction. In our experiment, the frictional behavior of the ceramic pressure media does not allow for precise pressure adjustment after the initial compression and heating phase, therefore we chose not to modify the experimental pressure between deformation sequences beyond the automatic feedback system that maintains a constant oil pressure. By not modifying the pressure during the experiment, a slight pressure increase occurred as the temperature was increased in each subsequent deformation sequence.

For experiments San_381 and San_416, X-ray spectra were collected at the starting condition, and then the D-DIA differential rams were advanced to deform the samples while diffraction, radiographic, and ultrasonic measurements were made sequentially. In deformation sequence 3 of San_381 and all deformation sequences of San_416, the sense of motion of the D-DIA rams was immediately reversed upon reaching the desired amount of strain and diffraction, radiographic, and ultrasonic measurements were made sequentially until the differential stress was released.

In experiment San_381, the sample was uniaxially deformed at 3.2–4.9 GPa at a nominal strain rate of $\sim 3.5 \times 10^{-6}$ sec^{-1} at 450°, 650°, 800°, and 950°C in four deformation sequences. In each sequence the sample was deformed ~2–5%, and then with the exception of sequence 3 as described above, the D-DIA motors for the differential rams were stopped. The temperature was then raised to 900°C and the differential rams were retracted at a nominal strain rate of $\sim 1 \times 10^{-6}$ to release the differential stress. This was then followed by an additional period of stress relaxation.

In experiment San_416, the sample was uniaxially deformed at 7.8–10.5 GPa and 450°, 650°, and 900°C in three deformation sequences. The sample was deformed ~2.5%–4%, and then the D-DIA motors for the differential rams were retracted until the differential stress was released. Applying a uniaxial load resulted in a nominal strain rate of 3.2×10^{-6} sec^{-1} during differential ram advancement, followed by a nominal strain rate of 0.9×10^{-6} sec^{-1} as the differential rams were retracted.

2.3. Data Analysis

2.3.1. Measurements of Sample Strain

X-radiographic images of the sample were obtained at six-minute intervals during each deformation sequence. The X-ray absorption contrast between the sample and the metal foils placed at its interfaces allows the sample to be identified and the length to be measured during the experiment. We then compare the intensity profiles of the first photo in each deformation sequence with the subsequent photos to determine the amount of sample strain. We determined the sample length, in pixels, for the X-radiographic image prior to pressurization using the open-source software *ImageJ* (Abràmoff et al., 2004); this was done to create a pixel to micron conversion using the known initial sample length. The pixel to micron conversion allowed us to determine the starting length of the first photo in each deformation sequence with ~0.3% precision. The radiographs were not taken simultaneously with diffraction or ultrasonic measurements; therefore, sample strain (ε) as a function of time elapsed was fit with a polynomial function to allow for the calculation of the sample strain at the time of each diffraction and ultrasonic measurement. The sample length during deformation $\left(l\right)$ at the time of the ultrasonic wave measurements was then calculated using the sample strain and the sample length, in microns, prior to deformation $\left(l_0\right)$ in each deformation sequence:

$$l = \left(\left(\varepsilon * l_0\right) + l_0\right) \tag{5}$$

A polynomial function was chosen to fit the sample strain versus time data as opposed to a linear fit, due to the observed sluggishness in the system at the start of deformation (see Table S1 in the Supporting Information S1 for strain rate information of each deformation sequence).

2.3.2. Diffraction Measurements

Powder diffraction patterns were taken at six minute intervals alternating between collection from the sample and the alumina buffer rod using an array of 10 energy-dispersive detectors. The primary detectors used in our data analysis procedure measured diffraction parallel and perpendicular to the vertical compression axis. Two of these detectors are aligned along the compression axis at $\psi = 0°, 180°$ to obtain diffraction from lattice planes that are normal to compression (Figure S4 in the Supporting Information S1). A detector at $\psi = 90°$ is also used to obtain diffraction from lattice planes parallel to the compressive direction (Figure S4 in the Supporting Information S1). The lattice strain ($\varepsilon^{hkl}_{\text{lattice}}$) was calculated for each population of grains producing a diffraction peak as:

$$\varepsilon^{hkl}_{\text{lattice}} = \frac{d_h hkl - d_f hkl}{d_h hkl} \tag{6}$$

where $d_n hkl$ is the d-spacing measured for a grain population immediately before deformation at a given detector, and $d_f hkl$ is the d-spacing measured by a given detector during deformation. The lattice strain is a measure of the average stress on the population of grains producing the diffraction peak (Burnley & Zhang, 2008).

2.3.3. DIASCoPE: Directly Integrated Acoustic System Combined With Pressure Experiments

The DIASCoPE is an experimental acoustic system that allows for the measurement of elastic wave velocities during an in-situ high pressure experiment (Whitaker et al., 2017). The system uses ultrasonic interferometry to measure acoustic wave velocities and is integrated into the D-DIA and the 6-BM-B EPICS computing system which allows for automated collection of experimental measurements (see Figure S7 in the Supporting Information S1 for the communication path of the DIASCoPE system for ultrasonic measurements). A dual-mode 10° Y-cut $LiNbO_3$ piezoelectric transducer is attached to the bottom of the lower tungsten carbide anvil (Figure 2). The transducer was used to transmit frequencies and receive the reflections for collection of nearly synchronous *P*- and *S*-wave measurements during the experiment. The

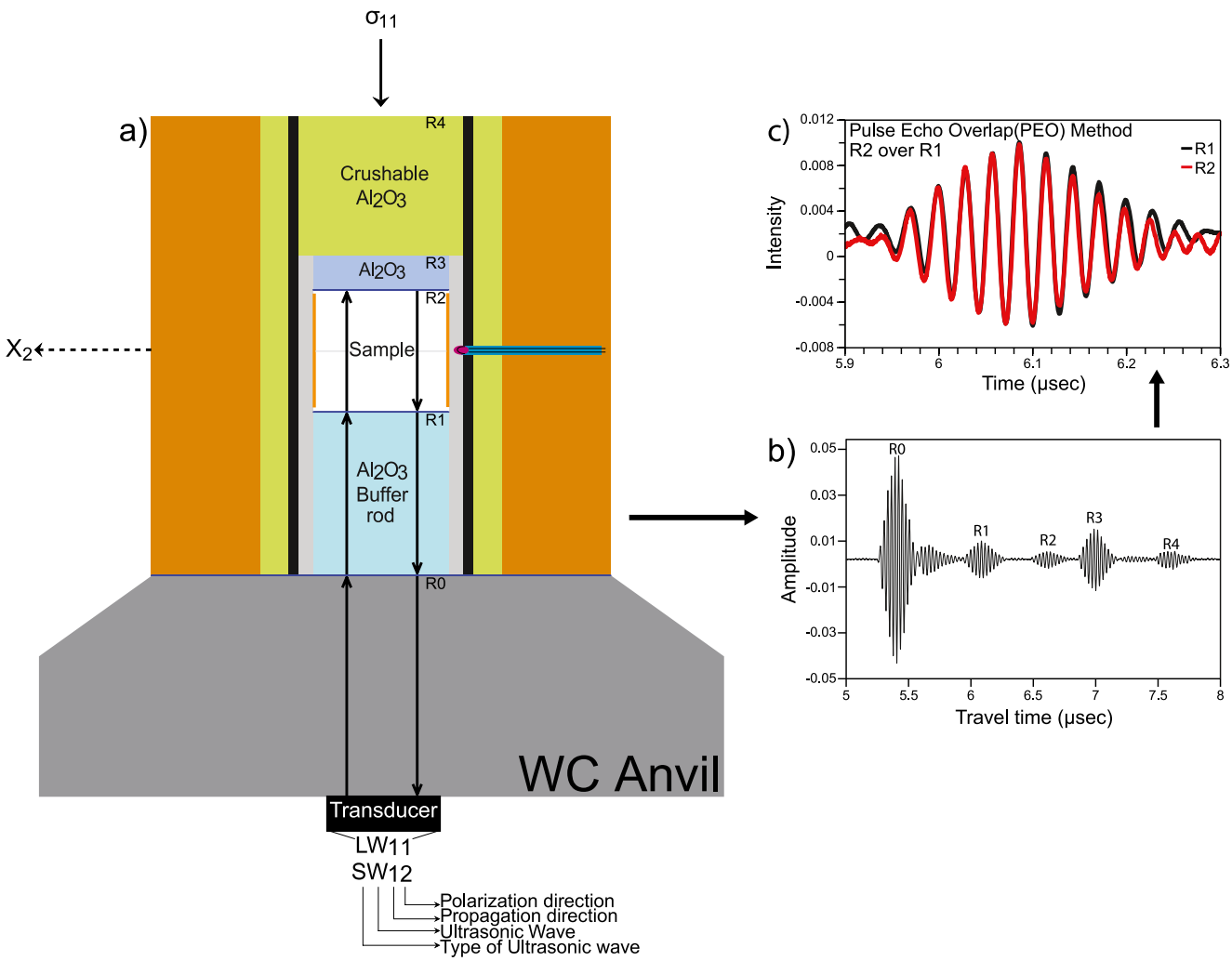

Figure 2. (a) A transducer attached to the bottom anvil transmits an ultrasonic wave pulse (optimal for *P*- or *S*-wave) and the reflection from the contact between different materials is recorded. (R0) is the reflection off of the lower anvil-buffer rod interface, (R1) buffer rod-sample interface, (R2) sample-above sintered Al_2O_3 piston interface, (R3) sintered Al_2O_3 piston-crushable Al_2O_3 piston interface, and (R4) crushable Al_2O_3 piston-upper anvil interface. Note-The sample size is typically 1–2 mm in length. Refer to the supplementary text for more information on the cell assembly measurements. (b) The observed acoustic signal recorded for file SAN_416_0033.udat in experiment San_416 for a 35 MHz wave pulse that generated *S*-waves. The amplitude of the reflections from various material interfaces is shown as a function of time. (c) The pulse-echo-overlap method is used to determine the travel time in the sample by overlaying the (R2) reflection on the (R1) reflection and measuring the time offset (After Whitaker et al., 2017).

Table 1
Comparison of the Acoustoelastic Constants for P- and S-Wave Velocities

Experiment		Seq.	Pressure (GPa)	Temperature[a] (°C)	Wave velocity (km/s)	A_{ij} advancement	A_{ij} retraction	σ^a
P-wave (A_{11})	San_381	1	3.2 (3)	451 (2)	7.99 (1)	1.05 (3)	–	1.82 (1)
		2	4.0 (3)	650 (2)	7.89 (1)	1.35 (5)	–	1.58 (1)
		3	4.4 (3)	804 (3)	7.72 (1)	0.47 (14)	1.06 (6)	1.35 (1)
		4	4.9 (3)	946 (3)	7.74 (1)	1.64 (20)	–	0.56 (1)
	San_416	1	7.8 (3)	449 (2)	8.80 (1)	0.75 (16)	0.598 (5)	2.37 (1)
		2	9.8 (3)	656 (3)	8.75 (1)	0.52 (3)	0.548 (8)	1.92 (1)
		3	10.5 (3)	898 (5)	8.57 (1)	0.77 (2)	0.62 (1)	1.54 (1)
S-wave (A_{12})	San_381	1	3.2 (3)	451 (2)	4.52 (1)	0.39 (4)	–	1.82 (1)
		2	4.0 (3)	650 (2)	4.46 (1)	−0.42 (2)	–	1.58 (1)
		3	4.4 (3)	804 (3)	4.35 (1)	−0.35 (7)	0.16 (5)	1.35 (1)
		4	4.9 (3)	946 (3)	4.35 (1)	0.17 (28)	–	0.56 (1)
	San_416	1	7.8 (3)	449 (2)	4.90 (1))	−0.111 (4)	−0.208 (4)	2.37 (1)
		2	9.8 (35)	656 (3)	4.84 (1)	−0.206 (9)	−0.207 (7)	1.92 (1)
		3	10.5 (3)	898 (5)	4.75 (1)	−0.175 (8)	−0.280 (4)	1.54 (1)

Note. The acoustoelastic constants are separated into "A_{ij} advancement" which represents the acoustoelastic constant during differential ram advancement, and "A_{ij} retraction" which represents the acoustoelastic constant during differential ram retraction. The macroscopic stress (σ^a) on the sample (in GPa) at 1.5% is shown.
[a]Systematic uncertainty of ±25°C.

transducer was set to a frequency of 35 MHz for *S*-waves and 60 MHz for *P*-waves. The pulse-echo-overlap method was implemented in Plot85, a data analysis software developed for the 6-BM-B beamline, to analyze the data and obtain the *P*- and *S*-wave travel times. The elastic wave velocities (V) were then calculated by dividing the distance the acoustic wave traveled in the sample by the two-way travel time (Δt):

$$V = \frac{2L}{\Delta t} \tag{7}$$

where L is the length of the sample. The uncertainty of the wave velocity measurements is a function of the uncertainty in the absolute length of the sample and the uncertainty in the measured travel time (~0.5 ns). See Figure S10 in the Supporting Information S1 for comparison of the wave velocity measurements determined for San Carlos olivine in this experiment with measurements from the literature.

2.4. Stress Determination From Elastic-Plastic Self-Consistent Modeling

EPSC modeling (Tomé & Oliver, 2002; Turner & Tomé, 1994) is a numerical modeling technique that can be used to interpret synchrotron X-ray diffraction measurements of lattice strain. Typically D-DIA studies have instead calculated the differential lattice strain, which is interpreted using a method that assumes a Reuss state of stress developed by Singh et al. (1998). However, other studies (Burnley, 2015; Burnley & Kaboli, 2019; Burnley & Zhang, 2008; Hilairet et al., 2012; Raterron et al., 2013) have shown that it does not suffice to look at this differential lattice strain to evaluate the macroscopic load due to the heterogeneous distribution of stress among grain populations within a polycrystalline aggregate. The EPSC model inputs include boundary conditions, crystal orientation, slip systems, single crystal elastic constants, and unit cell dimensions. We model the eight commonly observed slip systems in olivine, two unidirectional slip systems to simulate kink band formation (Burnley, 2015; Burnley & Kaboli, 2019; Kaboli et al., 2017), and an isotropic deformation mechanism composed of 30 slip planes (Burnley & Kaboli, 2019) to allow a small amount of anelastic deformation during the initial elastic portion of the experiment. Lattice strain versus sample strain curves were compared with the EPSC models to determine the macroscopic stress on the sample at

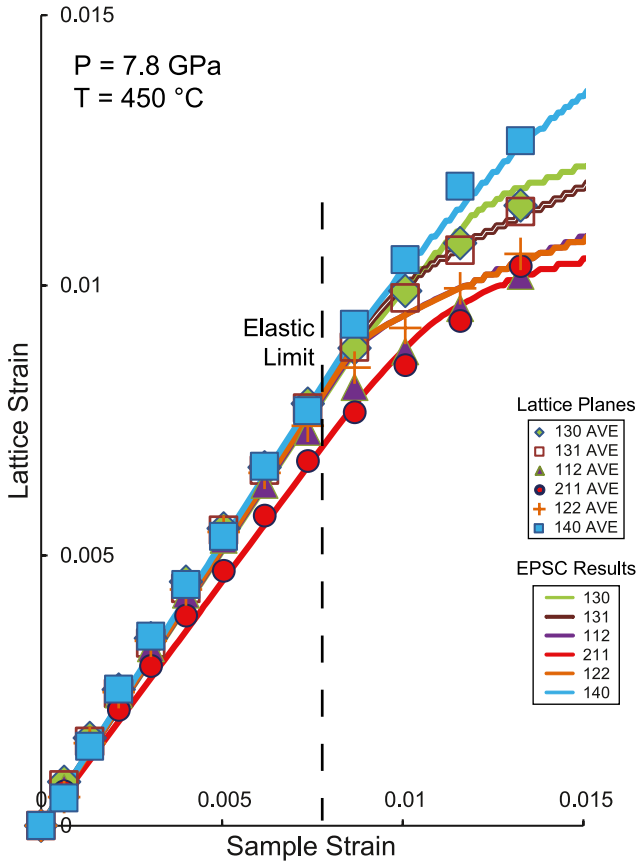

Figure 3. Lattice strain versus sample strain data (symbols) for deformation sequence 1 of San_416. The solid lines represent the elastic-plastic self-consistent model simulation lattice strain calculated to match the corresponding diffraction data. The vertical dashed line denotes the elastic limit. Data beyond the elastic limit is not used in calculation of the acoustoelastic constants.

any given time during the experiment (Figures S5 and S6 in the Supporting Information S1). For more information on the parameters used in the EPSC models, and the modeled diffraction data for each deformation sequence, see the supplementary information.

3. Results

Polycrystalline olivine samples were deformed up to 5% at pressure conditions ranging from 3.2–10.5 GPa and temperatures from 450–950°C (see Table 1). An example of lattice strain versus sample strain data is given in Figure 3 for deformation sequence 1 of San_416. The macroscopic stress values needed for the acoustoelastic constants are obtained from data within the elastic limit, which is indicated by the vertical dashed line on the figure. The stress values at 1.5% strain in each deformation experiment can be found in Table 1. For more information on the uncertainty of values in Table 1, see the supplementary information. The samples did not develop a significant preferred orientation during the experiments, with a J-index less than four for the recovered samples. Electron backscatter orientation image maps and measured preferred orientations are given in Figures S11–S14 in the Supporting Information S1.

$\Delta V/V$ for longitudinal and shear wave data is plotted as a function of macroscopic stress for deformation sequences 1 and 2 of San_381 and San_416 during differential ram advancement (Figure 4). The acoustoelastic constants are calculated from a linear regression of the data points within the elastic limit. We observe that the $\Delta V_p / V_p^0$ consistently increases with increased differential stress as seen by the positive acoustoelastic constant. The $\Delta V_s / V_s^0$ generally decreases slightly with increased differential stress, but is less sensitive to compression, with a slope trending near zero.

Figure 5 shows $\Delta V_p / V_p^0$ and $\Delta V_s / V_s^0$ as a function of macroscopic stress for deformation sequences 1, 2, and 3 of experiment San_416 during differential ram advancement and retraction. The acoustoelastic slopes during advancement to the elastic limit and retraction follow a similar slope in the *P*-wave data, and in the *S*-wave data.

The acoustoelastic constants for *P*- and *S*-wave data are plotted as a function of pressure and temperature in Figure 6. We do not observe temperature dependence, but minor pressure dependence can be seen. When the temperature is comparable, it is observed that an increase in pressure results in a decrease in the A_{11} acoustoelastic constants. The experimental pressure and temperature conditions, wave velocity at hydrostatic stress, and the acoustoelastic constants during differential ram advancement and retraction for each deformation sequence are given in Table 1.

4. Discussion

4.1. Acoustoelastic Constants

4.1.1. Sensitivity of Acoustoelastic Constants

We observe that the acoustoelastic constant for the P-wave propagating along the axis of compression (A_{11}) has a greater sensitivity to compression than the *S*-wave; this can be seen for other materials, including metals and concrete (Egle & Bray, 1976; Bompan & Haach, 2018; Lillamand et al., 2010). The values of A_{11} for experiment San_381 are positive with an average uncertainty ±0.08; for San_416, the A_{11} values are positive with an average uncertainty of ±0.027. The *S*-wave propagating along the axis of compression (A_{12}) shows less sensitivity to compression with values trending near zero. The values of A_{12} for experiment San_381

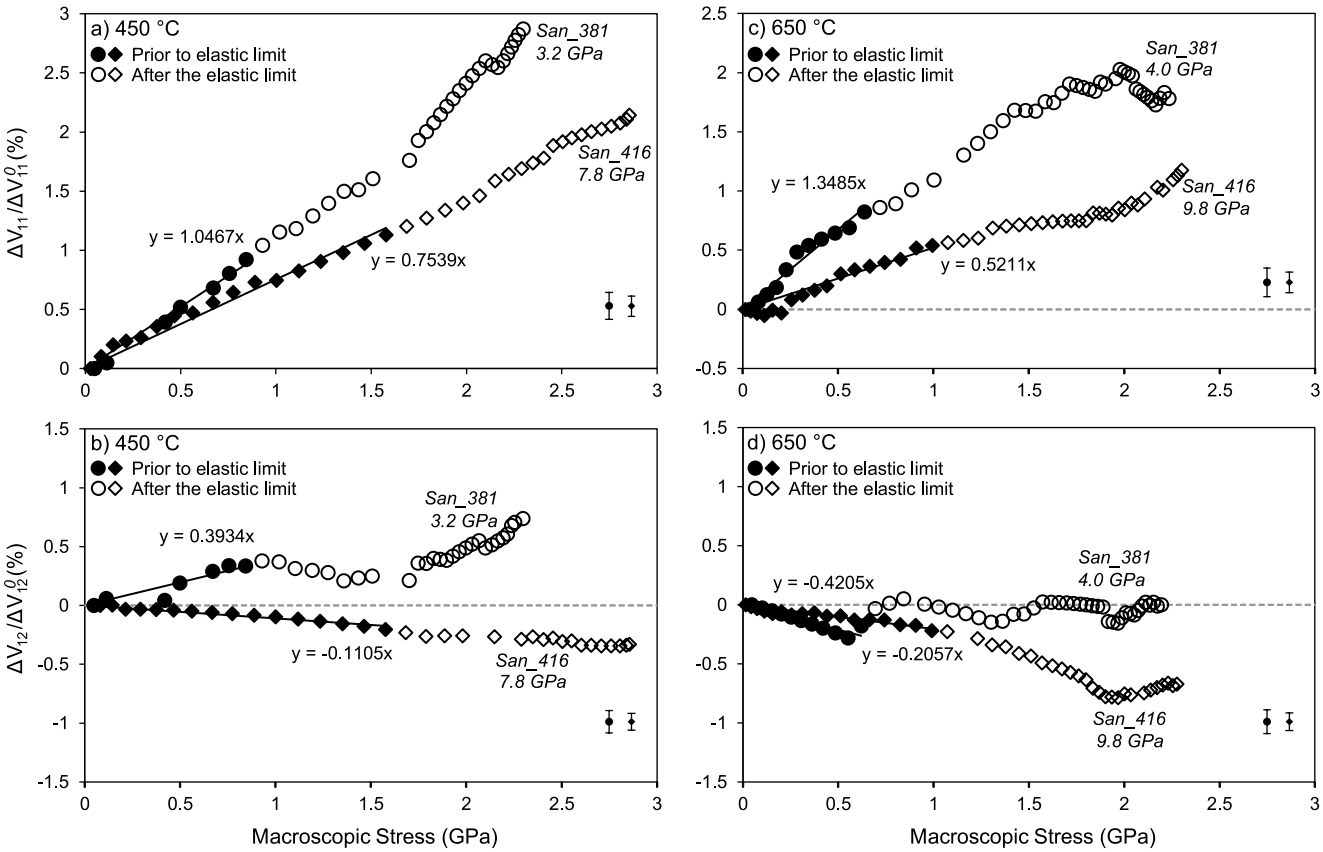

Figure 4. Comparison of acoustoelastic slope shown as the relative wave velocity change (ΔV_{ij} / V_{ij}^0) as a function of the macroscopic stress (in GPa) for the first deformation sequence in San_381 (P = 3.2 GPa) and San_416 (P = 7.8 GPa) at ~450°C (a, b), and second deformation sequence in San_381 (P = 4.0 GPa) and San_416 (P = 9.8 GPa) at ~650°C (c, d). Figures 4a and 4c show the P-wave (V_{11}) data and Figures 4b and 4d show the S-wave (V_{12}) data.

data are both positive and negative with an average uncertainty ±0.07; for San_416, the A_{12} values are negative with an average uncertainty of ±0.01.

4.1.2. Comparison of Differential Ram Advancement and Retraction Acoustoelastic Constants

We should expect that the $\Delta V/V$ and resulting acoustoelastic constants during differential ram advancement and retraction would be within error of each other, as this has been observed in other studies (Crecraft, 1967; Egle & Bray, 1976). However, we observe some differences. These differences are likely caused by two different aspects of our experiments and analysis procedure; potential pressure drift during the experiment and challenges with generating EPSC models for the retraction phase of the experiments.

While the difference in the acoustoelastic constants are smaller as is reflected in similar slopes between the advancement and retraction phases, the offset that is observed in the $\Delta V/V$ between the acoustoelastic slopes during differential ram advancement and retraction is more significant. In other words, with return to near hydrostatic state the wave velocity does not always return to the same value. Looking at the $\Delta V/V$ value in Figure 5, at near hydrostatic conditions for the differential ram retraction data, we can see that at 450°C the wave velocity upon return to near hydrostatic conditions is higher as indicated by the greater $\Delta V/V$ value, approximately the same return velocity at 650°C, and at 900°C the wave velocity is lower than the initial hydrostatic wave velocity (as indicated by the negative $\Delta V/V$ value). It should be noted that we assume that the pressure remains constant during each deformation cycle; however, a small fluctuation in pressure may cause this observed offset. The hysteresis in the internal pressure is consistent with how the temperature affects the relaxation in the cell assembly.

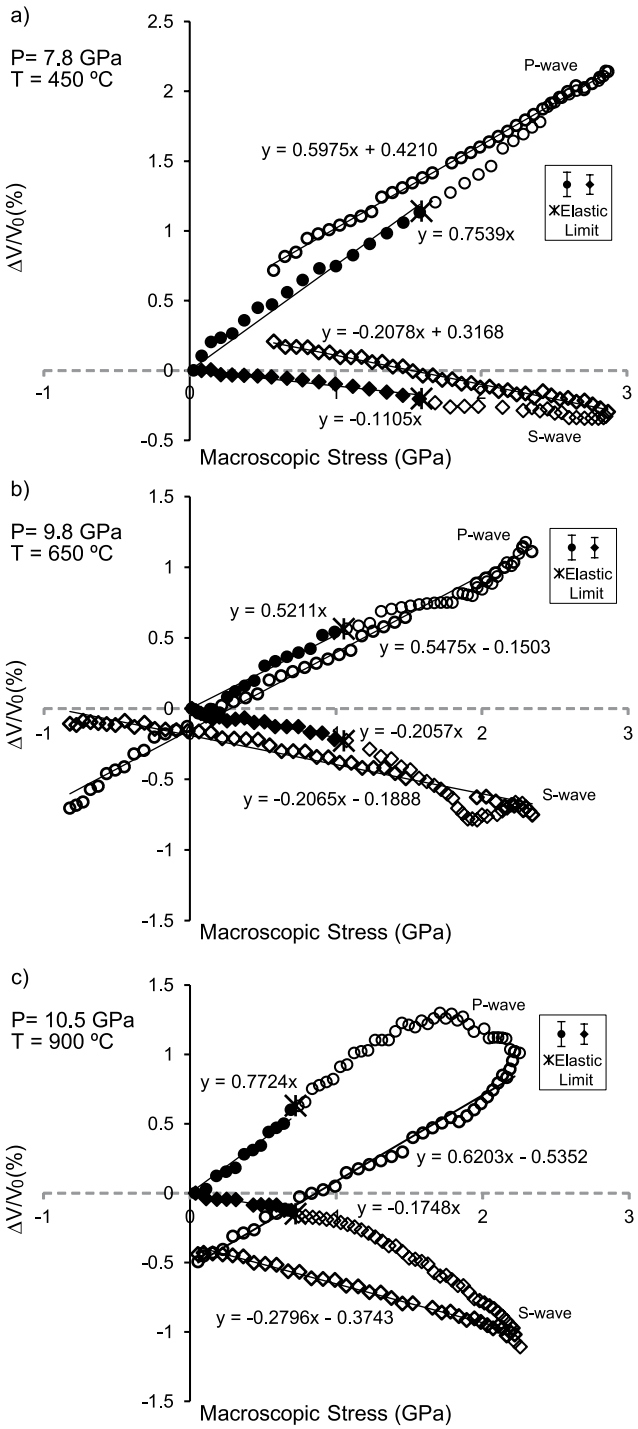

Figure 5. Comparison of acoustoelastic slope during differential ram advancement to the elastic limit and during differential ram retraction for San_416 deformation sequence (a) 1, (b) 2, and (c) 3. The shaded circles include data points used for calculating the A_{11} "advancement" acoustoelastic constant, and the shaded diamonds include data points used for calculating the A_{12} "advancement" acoustoelastic constant. The data used to determine the "retraction" acoustoelastic constant for *P*- and *S*-wave data is indicated by a trendline through the bolded data points. Pressure and temperature are denoted for each sequence.

The macroscopic stress used in calculating the acoustoelastic constants is determined through interpretation of our X-ray diffraction data using EPSC modeling. A poor fit toward the end of the plastic deformation phase during differential ram advancement will result in an offset during differential ram retraction between the diffraction data and the EPSC model (Figure S6 in the Supporting Information S1). However, since the slopes remain parallel this will only result in a minor discrepancy (<0.1%) in the acoustoelastic constant.

4.1.3. Acoustoelastic Constants Comparison With Literature

As this is the first measurement of the acoustoelastic constants at high pressure, there are no other comparable measurements with which to compare our results. However, it is informative to make comparisons with measurements of metals at low pressure. Most measurements in the metals literature report the third-order elastic constants rather than the acoustoelastic constants. Thus, through reordering of Equations 3a and 3b, the acoustoelastic constants, A_{11} and A_{12} respectively, can be determined as a function of the second- and third-order elastic constants:

$$A_{11} = -\left(\frac{1}{\left(2\left(\lambda+2\mu\right)\right)*\left(3\lambda+2\mu\right)}\right) * \left(\left(\frac{\lambda+\mu}{\mu}\right)*\left(4\lambda+10\mu+4m\right)+\lambda+2l\right) \quad (8a)$$

$$A_{12} = -\left(\frac{1}{\left(2\mu\right)*\left(3\lambda+2\mu\right)}\right)*\left(4\lambda+10\mu+m+\frac{\lambda n}{4\mu}\right) \quad (8b)$$

We include a negative sign in the acoustoelastic constant equations, as we define compression as positive. Table S5 in the Supporting Information S1 summarizes the second- and third-order elastic constants from various metals, concrete, and rock from the literature and the acoustoelastic constants calculated from Equations 8a–8b. We observe that the A_{11} and A_{12} values for polycrystalline San Carlos olivine at high confining pressure are closer to the range of A_{11} and A_{12} values for metals at low confining pressure than of those for rocks. This is not surprising since the acoustoelastic response for geologic materials at ambient to low confining pressure is attributed to pore closure and microcracks, which should not be as significant at high confining pressure conditions.

There is a clear relationship between the acoustoelastic constants and other material properties. Figure 7 shows the *P*- and *S*-wave acoustoelastic constants of various materials from the literature as a function of the bulk modulus and shear modulus, respectively. We observe a logarithmic decrease in the A_{11} acoustoelastic constant as a function of bulk modulus increase, with the values of the polycrystalline olivine samples of this study plotting in the range of other metallic materials. Similarly, when plotting the A_{12} acoustoelastic constant as a function of the shear modulus, a decrease in A_{12} is observed with shear modulus increase, and the polycrystalline olivine values are within the range of other metallic materials.

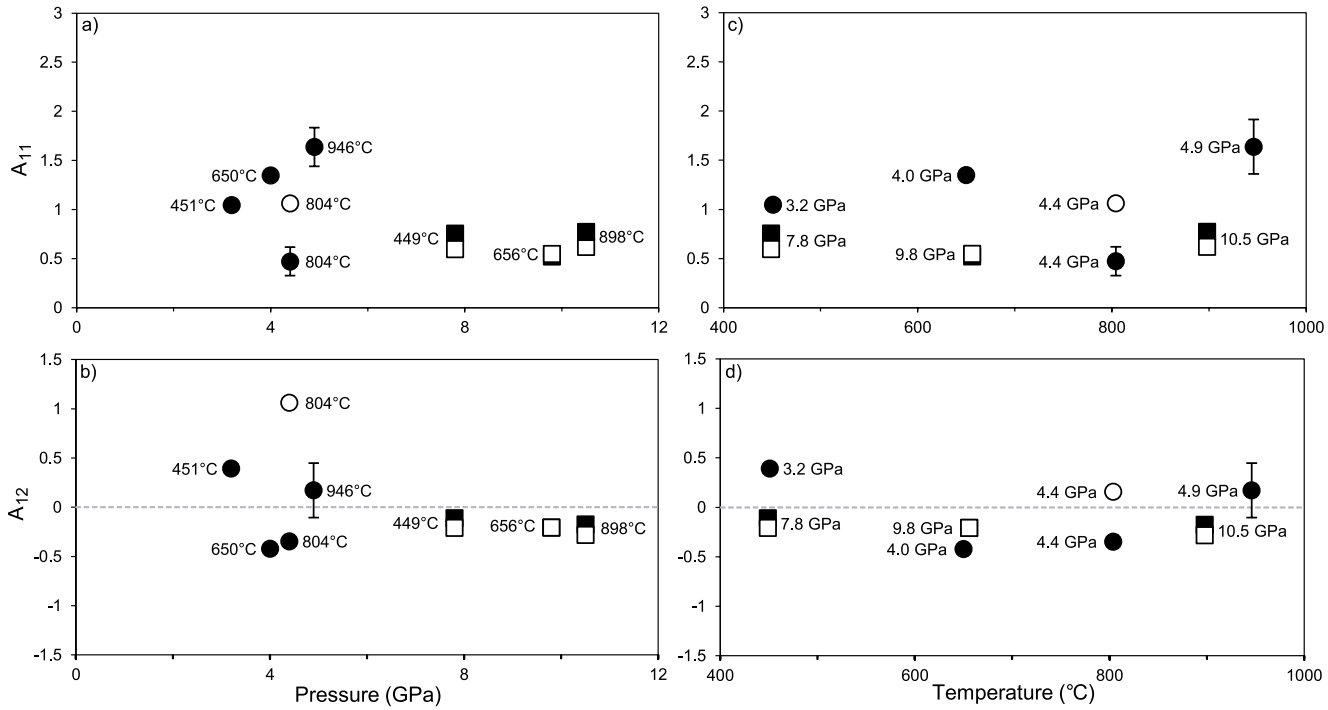

Figure 6. Acoustoelastic constants as a function of pressure (a and b) and temperature (c and d) for San_381 and San_416. The temperature and pressure conditions of each deformation sequence is listed next to the corresponding data point. A_{11} and A_{12} are the acoustoelastic constants for the *P*- and *S*-wave, respectively. Circle symbols denote San_381 data and square symbols denote San_416 data. Black symbols indicate A_{ij} advancement and white symbols indicate A_{ij} retraction. For most data points the error bars are within the symbols, for more information on the acoustoelastic constant uncertainty see Table 1.

4.2. Implications

A linear relationship is observed between the relative percentage of wave velocity change and stress up to the elastic limit. Additionally, at the onset of plastic deformation the linearity between $\Delta V/V$ and the macroscopic stress for the *P*-wave and *S*-wave data show a consistent slope for a given percentage of strain. This relatively consistent slope suggests that acoustoelastic measurements may provide an alternative method for deriving stress in offline experiments with integrated ultrasonic data collection.

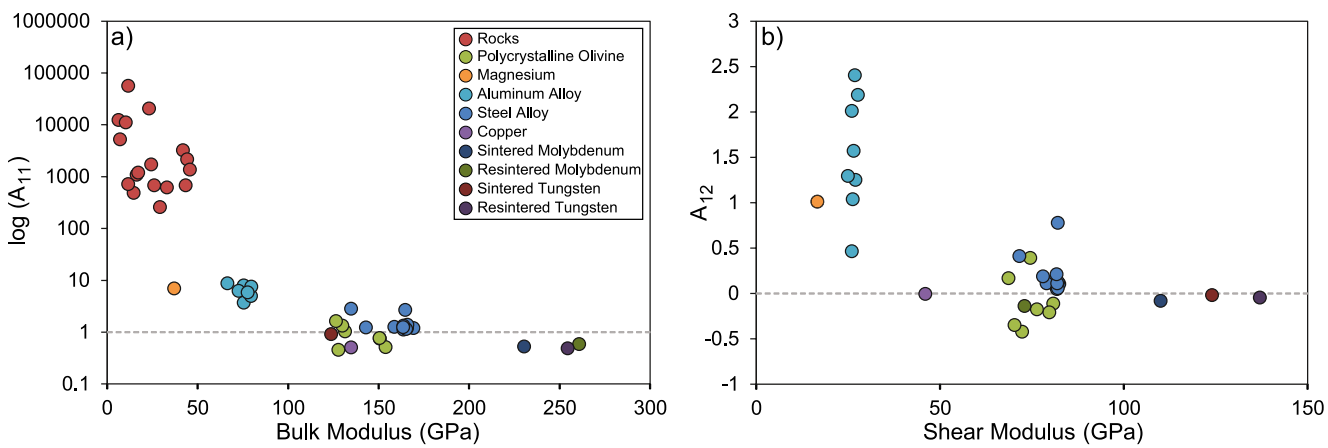

Figure 7. *P*-wave acoustoelastic constant (A_{11}) as a function of bulk modulus (a) and *S*-wave acoustoelastic constant (A_{12}) as a function of shear modulus (b) for the polycrystalline olivine samples of this study and various materials from the literature (metals- Ankay & Zhang, 2019; Crecraft, 1962, 1967; Egle & Bray, 1976; Hughes & Kelly, 1953; Nogueira, 2017; Smith et al., 1966; rocks at ambient to low confining pressure- Nur & Simmons, 1969; Rasolofosaon & Yin, 1996; Winkler & Liu, 1996; Zamora, 1990).

High resolution *P*-wave tomography studies of the upper mantle have shown a ±2% wave velocity change in the cold, stressed region of a subducting slab (Zhao et al., 2017). Therefore, a 0.5%–1% wave velocity change may occur for the level of stress present in subducting slabs. Thus, the acoustoelastic effect may need to be considered in future high resolution seismic data interpretation of cold, highly stressed regions of the Earth's upper mantle, such as subduction zones.

5. Conclusions

The acoustoelastic effect allows us to observe the effect stress has on *P*- and *S*- wave velocities. Using a linearization of the equations by Hughes and Kelly (1953) we can observe this effect in a combined uniaxial deformation and ultrasonic experiment at a synchrotron beamline for *P*- and *S*-wave velocities propagating along the axis of compression. We observe that *P*-wave velocities increase with uniaxial compression, and *S*-wave velocities generally decrease with uniaxial compression. Our results agree with the second-order linear elasticity theory that the relative wave velocity changes are a linear function of the stress. Greater acoustoelastic sensitivity is observed for the *P*-wave propagating along the axis of compression, and the corresponding acoustoelastic constant, A_{11}, decreases slightly with pressure. These findings suggest that acoustoelastic measurements may need to be considered in seismic data interpretation and provide potential for the evaluation of stress through the relative wave velocity change in offline experiments.

Data Availability Statement

Data sets for this research are made available in the Dryad repository: https://doi.org/10.5061/dryad.98sf7m0jn.

Acknowledgments
This research was supported by a grant from the National Science Foundation under award NSF-EAR13613399, and by the National Nuclear Security Administration under the Stewardship Science Academic Alliances program through Department of Energy (DOE) Cooperative Agreement #DE-NA0001982. This research used resources of the Advanced Photon Source, a U.S. Department of Energy Office of Science User Facility operated for the DOE Office of Science by Argonne National Laboratory under Contract No. DE-AC02-06CH11357. Use of the 6-BM-B beamline was supported by COMPRES, the Consortium for Materials Properties Research in Earth Sciences, under NSF Cooperative Agreement No. EAR 16–61511 and by the Mineral Physics Institute, Department of Geosciences, Stony Brook University. We thank Carrie Clark and Dawn Reynoso for assistance with data analysis as well as Shirin Kaboli and Haiyan Chen for assistance on the beamline. We would also like to thank the two anonymous reviewers for the thoughtful comments that helped us improve this paper.

References

Abràmoff, M. D., Paulo, J. M., & Sunanda, J. R. (2004). Image processing with ImageJ. *Biophotonics International*, *11*, 36–42.
Ankay, B., & Zhang, C. (2019). Acoustoelastic evaluation of ultra-high performance concretes. *AIP Conference Proceedings*, *2102*, 110002. https://doi.org/10.1063/1.5099839
Bateman, T., Mason, W. P., & McSkimin, H. J. (1961). Third-order elastic moduli of germanium. *Journal of Applied Physics*, *32*, 928–936. https://doi.org/10.1063/1.1736135
Benson, R. W., & Raelson, V. J. (1959). From ultrasonics to a new stress-analysis technique. *Product Engineering*, *30*, 56–59. https://doi.org/10.1080/00306525.1959.9633303
Bergman, R. H., & Shahbender, R. A. (1958). Effect of statically applied stresses on the velocity of propagation of ultrasonic waves. *Journal of Applied Physics*, *29*, 1736–1738. https://doi.org/10.1063/1.1723035
Birch, F. (1966). Compressibility; elastic constants. In Handbook of physical constants (pp. 97–174). Geological Society of America. https://doi.org/10.1130/mem97-p97
Bompan, K. F., & Haach, V. G. (2018). Ultrasonic tests in the evaluation of the stress level in concrete prisms based on the acoustoelasticity. *Construction and Building Materials*, *162*, 740–750. https://doi.org/10.1016/j.conbuildmat.2017.11.153
Burnley, P. C. (2015). Elastic plastic self-consistent (EPSC) modeling of plastic deformation in fayalite olivine. *American Mineralogist*, *100*, 1424–1433. https://doi.org/10.2138/am-2015-5234ccbyncnd
Burnley, P. C., & Kaboli, S. (2019). Elastic plastic self-consistent (EPSC) modeling of San Carlos olivine deformed in a D-DIA apparatus. *American Mineralogist*, *104*, 276–281. https://doi.org/10.2138/am-2019-6666
Burnley, P. C., & Zhang, D. (2008). Interpreting in-situ X-ray diffraction data from high pressure deformation experiments using elastic–plastic self-consistent models: An example using quartz. *Journal of Physics: Condensed Matter*, *20*, 285201. https://doi.org/10.1088/0953-8984/20/28/285201
Chaki, S., & Bourse, G. (2009). Stress level measurement in prestressed steel strands using acoustoelastic effect. *Experimental Mechanics*, *49*, 673–681. https://doi.org/10.1007/s11340-008-9174-9
Crecraft, D. I. (1962). Ultrasonic wave velocities in stressed nickel steel. *Nature*, *195*, 1193–1194. https://doi.org/10.1038/1951193a0
Crecraft, D. I. (1967). The measurement of applied and residual stresses in metals using ultrasonic waves. *Journal of Sound and Vibration*, *5*, 173–192. https://doi.org/10.1016/0022-460X(67)90186-1
Dey, S., Roy, N., & Dutta, A. (1984). *P* and *S* waves in a medium under initial stresses and under gravity. *Indian Journal of Pure and Applied Mathematics*, *15*, 795–808.
Durham, W. B., Weidner, D. J., Karato, S., & Wang, Y. (2002). New developments in deformation experiments at high pressure. *Reviews in Mineralogy and Geochemistry*, *51*, 21–49. https://doi.org/10.2138/gsrmg.51.1.21
Egle, D. M., & Bray, D. E. (1976). Measurement of acoustoelastic and third-order elastic constants for rail steel. *Journal of the Acoustical Society of America*, *60*, 741–744. https://doi.org/10.1121/1.381146
Hilairet, N., Wang, Y., Sanehira, T., Merkel, S., & Mei, S. (2012). Deformation of olivine under mantle conditions: An in situ high-pressure, high-temperature study using monochromatic synchrotron radiation. *Journal of Geophysical Research*, *117*, B01203. https://doi.org/10.1029/2011jb008498
Hughes, D. S., & Kelly, J. L. (1953). Second-order elastic deformation of solids. *Physical Review*, *92*, 1145–1149. https://doi.org/10.1103/physrev.92.1145

Johnson, G. C. (1981). Acoustoelastic theory for elastic–plastic materials. *Journal of the Acoustical Society of America*, *70*, 591–595. https://doi.org/10.1121/1.386748
Johnson, G. C., Holt, A. C., Cunningham, B., & Cunningham, B. (1986). An ultrasonic method for determining axial stress in bolts. *Journal of Testing and Evaluation*, *14*, 253–259. https://doi.org/10.1520/jte10337j
Johnson, P. A., & Rasolofosaon, P. N. J. (1996). Nonlinear elasticity and stress-induced anisotropy in rock. *Journal of Geophysical Research*, *101*, 3113–3124. https://doi.org/10.1029/95jb02880
Kaboli, S., Burnley, P. C., Xia, G., & Green, H. W. (2017). Pressure dependence of creep in forsterite olivine: Comparison of measurements from the D-DIA and Griggs apparatus. *Geophysical Research Letters*, *44*, 10939–10947. https://doi.org/10.1002/2017gl075177
Li, B., Kung, J., & Liebermann, R. C. (2004). Modern techniques in measuring elasticity of Earth materials at high pressure and high temperature using ultrasonic interferometry in conjunction with synchrotron X-radiation in multi-anvil apparatus. *Physics of the Earth and Planetary Interiors*, *143–144*, 559–574. https://doi.org/10.1016/s0031-9201(04)00088-3
Lillamand, I., Chaix, J.-F., Ploix, M.-A., & Garnier, V. (2010). Acoustoelastic effect in concrete material under uni-axial compressive loading. *NDT & E International*, *43*, 655–660. https://doi.org/10.1016/j.ndteint.2010.07.001
Liu, J. X., Cui, Z. W., & Wang, K. X. (2007). Reflection and transmission of acoustic waves at the interface between rocks in the presence of elastic–plastic deformations. *Journal of Geophysics and Engineering*, *4*, 232–241. https://doi.org/10.1088/1742-2132/4/2/012
Lucet, N. (1989). Velocity and attenuation of sonic and ultrasonic waves in rocks under confining pressure (Doctoral dissertation). Paris Diderot University.
Man, C. S., & Lu, W. Y. (1987). Towards an acoustoelastic theory for measurement of residual stress. *Journal of Elasticity*, *17*, 159–182. https://doi.org/10.1007/bf00043022
Murnaghan, F. D. (1951). *Finite deformation of an elastic solid*. John Wiley.
Nogueira, C. L. (2017). Ultrasonic evaluation of acoustoelastic parameters in aluminum. *Journal of Materials in Civil Engineering*, *29*, 04017158. https://doi.org/10.1061/(ASCE)MT.1943-5533.0002009
Nur, A., & Simmons, G. (1969). Stress-induced velocity anisotropy in rock. *Journal of Geophysical Research*, *74*, 6667–6674. https://doi.org/10.1029/JB074i027p06667
Rasolofosaon, P. N. J., & Yin, H. (1996). Simultaneous characterization of anisotropy and nonlinearity in arbitrary elastic media: Reflections on experimental data. *Seismic Anisotropy*, 141–179. https://doi.org/10.1190/1.9781560802693.ch6
Raterron, P., Merkel, S., & Holyoke, C. W., III (2013). Axial temperature gradient and stress measurements in the deformation-DIA cell using alumina pistons. *Review of Scientific Instruments*, *84*, 043906. https://doi.org/10.1063/1.4801956
Rollins, F. R., Jr., Kobett, D. R., & Jones, J. L. (1963). Study of ultrasonic methods for nondestructive measurement of residual stress, part 2. (Technical report WADD-TR-61-42, 1–38). Midwest Research Institute.
Singh, A. K., Balasingh, C., Mao, H.-K., Hemley, R. J., & Shu, J. (1998). Analysis of lattice strains measured under nonhydrostatic pressure. *Journal of Applied Physics*, *83*, 7567–7575. https://doi.org/10.1063/1.367872
Smith, R. (1963). Stress-induced anisotropy in solids-the acousto-elastic effect. *Ultrasonics*, *1*, 135–147. https://doi.org/10.1016/0041-624x(63)90003-9
Smith, R. T., Stern, R., & Stephens, R. W. B. (1966). Third-order elastic moduli of polycrystalline metals from ultrasonic velocity measurements. *Journal of the Acoustical Society of America*, *40*, 1002–1008. https://doi.org/10.1121/1.1910179
Thurston, R. N., & Brugger, K. (1964). Third-order elastic constants and the velocity of small amplitude elastic waves in homogeneously stressed media. *Physical Review*, *135*, AB3. https://doi.org/10.1103/physrev.135.ab3.2
Tomé, C. N., & Oliver, E. C. (2002). Code elasto-plastic self-consistent (EPSC). Los Alamos National Laboratory.
Toupin, R. A., & Bernstein, B. (1961). Sound waves in deformed perfectly elastic materials: Acoustoelastic effect. *Journal of the Acoustical Society of America*, *33*, 216–225. https://doi.org/10.1121/1.1908623
Turner, P., & Tomé, C. (1994). A study of residual stresses in Zircaloy-2 with rod texture. *Acta Metallurgica et Materialia*, *42*, 4143–4153. https://doi.org/10.1016/0956-7151(94)90191-0
Wang, X., Chen, T., Qi, X., Zou, Y., Kung, J., Yu, T., et al. (2015). Acoustic travel time gauges for in-situ determination of pressure and temperature in multi-anvil apparatus. *Journal of Applied Physics*, *118*, 065901. https://doi.org/10.1063/1.4928147
Whitaker, M. L., Baldwin, K. J., & Huebsch, W. R. (2017). DIASCoPE: Directly integrated acoustic system combined with pressure experiments—A new method for fast acoustic velocity measurements at high pressure. *Review of Scientific Instruments*, *88*, 034901. https://doi.org/10.1063/1.4977596
Winkler, K. W., & Liu, X. (1996). Measurements of third-order elastic constants in rocks. *Journal of the Acoustical Society of America*, *100*, 1392–1398. https://doi.org/10.1121/1.415986
Xie, F., Ren, Y., Zhou, Y., Larose, E., & Baillet, L. (2018). Monitoring local changes in granite rock under biaxial test: A spatiotemporal imaging application with diffuse waves. *Journal of Geophysical Research: Solid Earth*, *123*, 2214–2227. https://doi.org/10.1002/2017JB014940
Zamora, M. (1990). Experimental study of the effect of the geometry of rock porosity on the velocities of elastic waves (Doctoral dissertation). Paris Diderot University.
Zhao, D., Fujisawa, M., & Toyokuni, G. (2017). Tomography of the subducting Pacific slab and the 2015 Bonin deepest earthquake (Mw 7.9). *Scientific Reports*, *7*, 1–8. https://doi.org/10.1038/srep44487

References From the Supporting Information

Abramson, E. H., Brown, J. M., Slutsky, L. J., & Zaug, J. (1997). The elastic constants of San Carlos olivine to 17 GPa. *Journal of Geophysical Research: Solid Earth*, *102*(B6), 12253–12263. https://doi.org/10.1029/97JB00682
Anderson, O. L., & Isaak, D. G. (1995). Elastic constants of mantle minerals at high temperature. In T. J. Ahrens (Ed.), *Mineral physics & crystallography: A handbook of physical constants* (pp. 64–97). https://doi.org/10.1029/RF002p0064
Darling, K. L., Gwanmesia, G. D., Kung, J., Li, B., & Liebermann, R. C. (2004). Ultrasonic measurements of the sound velocities in polycrystalline San Carlos olivine in multi-anvil, high-pressure apparatus. *Physics of the Earth and Planetary Interiors*, *143*, 19–31. https://doi.org/10.1016/j.pepi.2003.07.018
Fei, Y. (1995). Thermal expansion. In Mineral physics and crystallography: A handbook of physical constants (Vol. 2, pp. 29–44). https://doi.org/10.1029/RF002p0029
Gonzalez-Platas, J., Alvaro, M., Nestola, F., & Angel, R. (2016). EosFit7-GUI: A new graphical user interface for equation of state calculations, analyses and teaching. *Journal of Applied Crystallography*, *49*, 1377–1382. https://doi.org/10.1107/s1600576716008050

Hielscher, R., Silbermann, C. B., Schmidl, E., & Ihlemann, J. (2019). Denoising of crystal orientation maps. *Journal of Applied Crystallography*, *52*, 984–996. https://doi.org/10.1107/S1600576719009075

Isaak, D. G. (1992). High-temperature elasticity of iron-bearing olivines. *Journal of Geophysical Research*, *97*, 1871–1885. https://doi.org/10.1029/91JB02675

Knittle, E. (1995). Static compression measurements of equations of state. In Mineral physics and crystallography: A handbook of physical constants (Vol. 2, pp. 98–142). https://doi.org/10.1029/rf002p0098

Liu, W., Kung, J., & Li, B. (2005). Elasticity of San Carlos olivine to 8 GPa and 1073 K. *Geophysical Research Letters*, *32*, L16301. https://doi.org/10.1029/2005GL023453

Mao, Z., Fan, D., Lin, J. F., Yang, J., Tkachev, S. N., Zhuravlev, K., & Prakapenka, V. B. (2015). Elasticity of single-crystal olivine at high pressures and temperatures. *Earth and Planetary Science Letters*, *426*, 204–215. https://doi.org/10.1016/j.epsl.2015.06.045

Stobbe, D. M. (2005). Acoustoelasticity in 7075-T651 aluminum and dependence of third order elastic constants on fatigue damage (Master's thesis). Georgia Institute of Technology.

Wang, Y., Durham, W. B., Getting, I. C., & Weidner, D. J. (2003). The deformation-DIA: A new apparatus for high temperature triaxial deformation to pressures up to 15 GPa. *Review of Scientific Instruments*, *74*, 3002–3011. https://doi.org/10.1063/1.1570948

Webb, S. L. (1989). The elasticity of the upper mantle orthosilicates olivine and garnet to 3 GPa. *Physics and Chemistry of Minerals*, *16*, 684–692. https://doi.org/10.1007/BF00223318

Weidner, D. J., Vaughan, M. T., Wang, L., Long, H., Li, L., Dixon, N. A., & Durham, W. B. (2010). Precise stress measurements with white synchrotron x rays. *Review of Scientific Instruments*, *81*, 013903. https://doi.org/10.1063/1.3263760

Zha, C. S., Duffy, T. S., Downs, R. T., Mao, H. K., & Hemley, R. J. (1998). Brillouin scattering and X-ray diffraction of San Carlos olivine: Direct pressure determination to 32 GPa. *Earth and Planetary Science Letters*, *159*, 25–33. https://doi.org/10.1016/s0012-821x(98)00063-6

Zhang, J. S., & Bass, J. D. (2016). Sound velocities of olivine at high pressures and temperatures and the composition of Earth's upper mantle. *Geophysical Research Letters*, *43*, 9611–9618. https://doi.org/10.1002/2016GL069949